Nanoscale Advances

PAPER

View Article Online
View Journal | View Issue

Cite this: *Nanoscale Adv.*, 2019, **1**, 3660

Development of a near infrared Au–Ag bimetallic nanocluster for ultrasensitive detection of toxic Pb^{2+} ions *in vitro* and inside cells†

Achinta Sannigrahi,‡[a] Sourav Chowdhury,‡[ab] Indrani Nandi,‡[ac] Dwipanjan Sanyal,[a] Sayantani Chall*[a] and Krishnananda Chattopadhyay *[ac]

Received 25th July 2019
Accepted 29th July 2019

DOI: 10.1039/c9na00459a

rsc.li/nanoscale-advances

Although the research activities pertaining to the synthesis of fluorescent noble metal nanoclusters (NCs) and their applications in biological optics have been growing, only limited information is available in the near IR (NIR) region. However, fluorescence spectroscopy and microscopy in the NIR region offer significant advantages over UV and visible wavelengths. In this manuscript, we demonstrate bio-mineralized synthesis of stable Au–Ag bimetallic NCs with tunable NIR fluorescence using bovine serum albumin (BSA) as a protein template. We also demonstrate its application in the detection of toxic heavy metal ions Pb^{2+} *in vitro* and inside cells. The tunability of the fluorescence emission between 680 nm and 815 nm is achieved by systematically varying the ratio of Au and Ag in the composite NCs. The bimetallic NCs when interacting with Pb^{2+} offered a large increase in fluorescence intensity, which enabled sensitive detection of Pb^{2+}. We determined a limit of detection (LOD) of 96 nM for the detection of Pb^{2+} under *in vitro* conditions, which is significantly less than the safe level in drinking water. Its applicability has also been demonstrated successfully in real water samples collected from local water bodies.

Introduction

Developing analytical approaches for the determination and sensing of heavy metal ions has been an exciting field of research, in which the most convenient ones are fluorescence based measurements.[1] This is because of the high sensitivity, quick analysis capability and generally non-invasive nature of fluorescence detection.[2–4] The primary interest lies in the synthesis of composite fluorescent materials, including metal based nanoclusters (NCs), which offer excellent biological compatibility, low toxicity, and photostability.[5–8] Interestingly, somewhat limited applications are available in current literature in the NIR wavelength region, although NIR fluorescence is advantageous for biological microscopy. The benefits of NIR come from its low background auto-fluorescence, less photo-damage and channel crosstalk.[9,10] Some of the recent developments of gold nanoclusters (Au NCs) in the NIR region include the preparation of trypsin stabilized NIR emissive Au NCs by Liu and co-workers[11] and thiolate protected Au NCs by Pramanik *et al.*[12] However, according to the 'energy gap law', it is challenging to prepare Au NCs with emission wavelength in the NIR region with high quantum yield (QY) through consecutive optimization of non-radiative pathways, which decrease emission energy.[11]

One promising strategy to increase QYs would involve doping of the Au core with precise numbers of silver (Ag) atoms.[12] Very recently, Wang *et al.* synthesized and structurally resolved X-ray diffraction of two mixed products of Ag/Au NCs. Pang *et al.* reported that lysozyme stabilized Au–Ag nanoclusters emit at 665 nm[13] whereas Mohanty *et al.* reported NIR emission at 707 nm by BSA stabilized Au–Ag nanoclusters.[7] Ag is a convenient metal for optical studies due to the advantageous position of *d*-electrons as compared to Au. Visible fluorescence from small bare clusters of Au and Ag atoms offer strong size dependence that has been successfully modelled using the electronic states in the metal cluster core. Interestingly, NIR fluorescence from ligated molecular metal nanoparticles does not exhibit strong size dependence and has not been modelled successfully.[14]

[a]*Structural Biology & Bio-Informatics Division, CSIR-Indian Institute of Chemical Biology, 4, Raja S. C. Mallick Road, Kolkata 700032, India. E-mail: krish@iicb.res.in; sayantani.chall@yahoo.com*

[b]*Department of Chemistry and Chemical Biology, Harvard University, 12, Oxford Street, Cambridge Massachusetts, USA*

[c]*Academy of Scientific and Innovative Research (AcSIR), Ghaziabad 201002, India*

† Electronic supplementary information (ESI) available: Two additional tables describing the synthetic optimization in terms of Au/Ag molar ratio variations and time resolved study with respect to Au/Ag variation have been mentioned. Absorption spectra of $(Au–Ag@BSA)_{opt}$ NCs; MALDI mass spectrum of the nanoclusters; X-ray photoelectron spectra; fluorescence stability of nanoclusters in the presence of EDTA, NaCl and different pH; stability of $(Au–Ag@BSA)_{opt}$ NCs with time; variation of nanocluster fluorescence intensity with increasing Ag concentration. See DOI: 10.1039/c9na00459a

‡ Contributed equally.

Different factors modulate the optical and biological properties of nanoscale materials.[15–18] For example, using site-directed mutagenesis and optical spectroscopy, our laboratory has shown recently that the position of a cysteine residue in the primary sequence of a protein plays profound roles in the fluorescence properties of Au NCs.[15] We have also shown that the alteration of the global conformation (folded globular *vs.* aggregated amyloid form)[16] and a switch in the secondary structure (alpha helix *vs.* beta sheet) of a protein can modulate protein–nanomaterial interactions.[17] In the present study, we have systematically studied the effect of change in the extent of Au and Ag in an Au–Ag bimetallic NC system on the fluorescence properties. We chose the protein BSA as the scaffold. This protein is a convenient and widely studied matrix to reduce as well as stabilize metal clusters. The first objective of the present study is to develop, using steady state and time resolved fluorescence spectroscopy, an Au to Ag concentration ratio, which would provide optimum emission intensity (acceptably high quantum yield) in the NIR region. The second objective of this study is to investigate the application of NIR emission of the above ratio optimized Au–Ag bimetallic nanoclusters (Au–Ag@BSA NCs) as a non-invasive fluorescence detection method for Pb^{2+} heavy metal. We are interested in the detection of Pb^{2+} because poisoning induced by this metal in food and water has been considered as a major public health risk in developing countries.[19,20] Exposure of Pb^{2+} has adverse effects on the hematopoietic, renal, reproductive and central nervous systems followed by oxidative stress generation.

While developing this bimetallic detection system, we have noted that the interaction of the target molecule often quenches NC fluorescence.[21] Metal induced quenching is expected to limit the sensitivity as well as the applicability in imaging applications requiring the use of higher excitation power thereby inducing photo-damage. The bimetallic NCs developed and optimized in the present study do not suffer from this limitation. This is because the gradual increase of Pb^{2+} concentration causes an almost ten times increase of the fluorescence intensity of the optimized Au–Ag@BSA NCs. Similar fluorescence increment is also observed during the detection of Pb^{2+} within cell cytosol media. Prior to live cell experiments, the MTT assay has been performed to ascertain cell viability. We have then extended the application of this as-prepared nanocluster to study samples collected from different local water sources.

Experimental

Materials

AR grade salt tetrachloroauric acid ($HAuCl_4$) and silver nitrate ($AgNO_3$, ≥99%) were purchased from Spectrochem (Mumbai, India). Sodium hydroxide (NaOH) beads were obtained from Merck (Darmstadt, Germany). Protein Bovine Serum Albumin (≥99%) was bought from Sigma Aldrich (St. Louis, USA). High purity water (≈18.2 MU) was used for the entire study. Various metal salts such as perchlorates of Na^+, K^+, Fe^{2+}, Fe^{3+}, Co^{2+}, Cd^{2+}, Hg^{2+}, Ni^{2+} and Zn^{2+} were purchased from Sigma-Aldrich (St. Louis, USA) and used as received. Other metal salts like $LiNO_3$, $Al(NO_3)_3$, $Pb(NO_3)_2$, $CrCl_3$, $MnCl_2$ and $Cu(ClO_4)_2$ were of the highest purity grade.

One pot synthesis of Au–Ag@BSA NCs

Synthesis of protein stabilized monometallic fluorescent NCs was reported by various groups.[6,7] In a typical synthesis process, red emissive Au–Ag@BSA NCs were prepared by mixing 2.5 mL of 10 mM Au salt solution and 8.6 mM Ag solution with 2.5 mL of BSA (20 mg mL^{-1}) under vigorous stirring at 37 °C for 20 hours. The molar concentration ratios of Au and Ag salts were varied keeping the total volume unchanged. Table S1† presents the corresponding volume ratio, molar ratio and expected atomic ratio of Au and Ag in the as-prepared product, assuming that all the Ag and Au ions were reduced to their zero valent states. The optimized molar ratio was found to be 2.3 : 2.0 which yielded bimetallic nanoclusters with the maximum fluorescence emission wavelength of 718 nm. The effective pH was 11 for the synthesis of the desired NCs. A very prominent color change was observed with varying molar ratios of Au and Ag. Accordingly, visual color changes of the final solutions were also very distinctive. Final purification of the as-prepared samples was carried out *via* centrifugation, which was followed by dialysis. The final solutions were stored at 4 °C for further experiments.

Characterization of Au–Ag@BSA NCs

Formation of the Au–Ag@BSA NCs was initially characterized by absorption (200–700 nm) and fluorescence studies using a Lambda 35 scan UV-visible spectrophotometer (PerkinElmer, Waltham, USA) and PTI fluorimeter (Photon Technology International, USA), respectively. The fluorescence emission spectra were recorded using an excitation wavelength of 490 nm. Fluorescence lifetimes were determined from time-resolved intensity decay by the method of time correlated single-photon counting using a nanosecond diode LED at 490 nm (IBH, nanoLED-07) as the light source. The data stored in a multichannel analyzer were routinely transferred to IBH DAS-6 decay analysis software. For all lifetime measurements, the fluorescence decay curves were analyzed using the bi-exponential iterative fitting program provided by IBH as in eqn (1)[22]

$$F(t) = \sum_i a_i \exp\left(-\frac{t}{\tau_i}\right) \quad (1)$$

where a_i is the pre-exponential factor representing the fractional contribution to the time resolved decay of the component with lifetime τ_i. Average lifetimes $\langle\tau\rangle$ for bi-exponential decays of fluorescence were calculated from the decay times and pre-exponential factors using eqn (2),[23]

$$\langle\tau\rangle = \frac{\alpha_1\tau_1 + \alpha_2\tau_2}{\alpha_1 + \alpha_2} \quad (2)$$

All fluorescence spectra were corrected with respect to instrumental response. All measurements were done repeatedly and reproducible results were obtained. The quantum yield

(QY) of the Au–Ag@BSA NCs was obtained by comparison with reference dye rhodamine B (in water), using eqn (3):[23]

$$QY_s = \frac{F_s \times A_r \times \eta_s \times QY_r}{F_r \times A_s \times \eta_r} \quad (3)$$

where, F_s and F_r are the integrated fluorescence emission of the sample and the reference. A_s and A_r are the absorbance at the excitation wavelength of the sample and the reference. QY_s and QY_r are the quantum yields of the sample and the reference, respectively. Rhodamine B was used as a reference dye (QY_r = 31% in water) to obtain the QY_s of Au–Ag@BSA NCs. The refractive indexes (η_r and η_s) of the solvent are 1.33 for both the reference and sample because water is used for both cases. All the experimental analyses were carried out at room temperature.

Matrix-assisted laser desorption ionization time-of-flight mass spectrometry (MALDI-TOF MS) (Applied Biosystems 4800 MALDI TOF/TOF) measurements of Au–Ag@BSA NCs were performed using sinapinic acid as a matrix. XPS measurements were done using an Omicron Nanotechnology (Omicron, Germany) instrument. The elemental composition was further confirmed by EDAX analysis using a HITACHI S-4800. A JEOL JEM-2100F transmission electron microscope (JEOL Ltd. Tokyo 196-8558, Japan) was used for obtaining TEM images. The sample was placed on a carbon-coated Cu grid, dried and analyzed for size evaluation. The zeta potential and hydrodynamic diameter were measured by using a Zetasizer Nano-ZS (Malvern Instruments, UK) at 25 °C.

Selective detections of Pb^{2+} ions

Selective detections of Pb^{2+} ion were performed by using fluorescence spectroscopy. To an aliquot of Au–Ag@BSA NCs various metal ion (*e.g.*, Na^+, K^+, Li^+, Al^{3+}, Mn^{2+}, Fe^{2+}, Fe^{3+}, Cr^{3+}, Co^{2+}, Cd^{2+}, Hg^{2+}, Pb^{2+}, Ni^{2+}, As^{3+}, Cu^{2+} and Zn^{2+}) solutions were added gradually and the corresponding change in fluorescence spectra was measured. With increased addition of lead ions, a significant increase of the fluorescence intensity of the nanocluster was observed which was insignificant or absent for other metal ions. 1 mM stock concentration of the metal salts was used for fluorescence titrations.

Cell culture and cell imaging

Cervical cancer cell line HeLa was used for live cell experiments. The cells were grown and maintained in Dulbecco's Modified Eagle's Medium (DMEM) supplemented with 10% heat-inactivated fetal bovine serum, 110 mg L^{-1} sodium pyruvate, 4 mM glutamine, 100 μg mL^{-1} penicillin, and 100 μg mL^{-1} streptomycin. Incubation was performed in humidified air containing 5% CO_2 at 37 °C. Cells were seeded in a 35 mm poly-D-lysine coated plate (MatTek Corporation, Ashland, MA) and grown up to ~75% confluency. To detect exogenous Pb^{2+} ions in the cell cytosol, cells were treated with 1 mM of Pb^{2+} ions. After an incubation period of 15 min, cells were subjected to thorough but gentle washing with PBS buffer in order to remove the unbound ions present in the media. Fresh media were added and again subsequently the cells were treated with Au–Ag@BSA NC solution (stock concentration 1 mM), which was incubated for 20 min in humidified air containing 5% CO_2 at 37 °C. Live cell confocal imaging was performed using an excitation wavelength of 488 nm using a Leica TCS-SP8 confocal microscope.

With an objective to gain a quantitative insight into the Au–Ag@BSA NC permeation within the cell cytoplasm and its complexation with Pb^{2+} ions within the cell cytosol, Java based image analysis bundle of ImageJ was applied. Spots showing fluorescence were randomly selected for obtaining preliminary insight into Au–Ag@BSA NC permeation. The pixel densities of these spots were compared with respect to the control set where no treatment was performed and hence no fluorescence was observed. Furthermore, a surface plot analysis output was obtained resorting to the surface plot plugin of ImageJ. The height of the plot presents the luminance of each pixel which constitutes the image. The 3D visualization was obtained resorting to the ImageJ 3D plugin. The final rendition offers a quantitatively precise post uptake residence rate of the Au–Ag@BSA NCs–Pb^{2+} complex.

MTT assay

The cellular cytotoxicity of the as-prepared Au–Ag@BSA NCs was studied using HeLa cells. The number of viable cells was determined using the MTT assay with 3-(4,5-dimethylthiazole-2-yl)-2,5-phenyltetrazolium bromide. The assay measures the proliferation rate of the cells. Only the viable cells reduce MTT to formazan crystals making use of the mitochondrial dehydrogenase enzyme. HeLa cells were seeded in 96-well plates keeping an optimal count of around 10^3 viable cells per well. The cells were incubated for 1 day. The viability assay was performed by incubating the cells with a series of Au–Ag@BSA NC concentrations, ranging from 500 nM to 1600 μM. After 20 min of treatment of cells with Au–Ag@BSA NCs, the media was replaced with the MTT containing media (1 mg mL^{-1}). The cells were thereafter incubated for a time frame of 4 h at an ambient temperature of 37 °C. The medium was finally removed and the cells were diluted in 100 μL of 0.04 N isopropyl alcohol. The relative formazan formation in each well was monitored by determination of absorbance at 540 nm using a microplate reader (MultiSkan, Thermo Scientific, USA). The resulting absorbance values were converted to percentage viability with respect to the untreated control cells.

Flow cytometry assay to monitor the extent of cellular permeation

The extent of cell cytosolic permeation of Au–Ag@BSA NCs was studied by using flow cytometry (FACS). This was considered important as the FACS output gives an authentic quantitative idea about the efficiency of cellular permeation in light of the fluorescence signal obtained from the uptaken probe.

A density of 10^7 cells was maintained for FACS measurements. As the MTT assay showed significantly higher viability of cells at probe concentrations spanning from 500 nM to 100 μM, we used FACS measurements on these concentrations of Au–Ag@BSA NCs. Cells were treated for 20 min and the incubation was carried out at 37 °C. FACS experiments were conducted on

BD FACSDiva. For all FACS-based permeation measurements, a 490 nm line was used for excitation using a 15 mW argon ion laser.

Results and discussion

Developing Au–Ag@BSA NCs with optimized NIR fluorescence intensity

Bimetallic fluorescent Au–Ag@BSA NCs were synthesized using BSA as the template. Each BSA monomer consists of 21 tyrosine and 35 cysteine residues, which can behave both as reducing and stabilizing agents.[24] It has been shown that at pH 12, tyrosine residues reduce metal ions to their respective zero valent states, while cysteine residues simultaneously stabilize and reduce the metal cluster through Au–S bond formation.[25] The synthesized Au–Ag@BSA NCs were first characterized using UV-visible absorption spectroscopy, which did not show any prominent peaks at 520 nm and 450 nm. The absorption peaks at 520 nm and 450 nm are characteristic of the presence of Au and Ag nanoparticles, respectively (with core diameter $\geq$ 2 nm) (Fig. S1a†).[26] However, a broad shoulder in the range 520–580 nm was found by UV-visible measurements (Fig. S1a† inset). The synthesized species also showed significant fluorescence intensity (as discussed later). The absence of prominent absorption peaks at 450 nm/520 nm and the presence of bright fluorescence emission indicated the formation of nanoclusters (and not nanoparticles). This inference is supported by previous reports.[6,27]

The first objective of this study was to develop a composite, which can provide optimum fluorescence emission wavelengths in the NIR region. In order to achieve this, we synthesized a number of Au–Ag@BSA NCs of varying Au : Ag molar ratios (4.5 : 0, 3.6 : 0.8, 2.7 : 1.6, 2.3 : 2.0, 1.8 : 2.4 and 0.9 : 3.1). In the case of BSA@Au NCs (in which there was no Ag), we found that they emitted with the maximum at 680 nm (λ_{ex} = 490 nm). However, with the increase in the extent of Ag, we observed a prominent shift of λ_{em} towards red to the NIR region (Fig. 1). Interestingly, Ag doping did not alter the excitation maximum of the composites and it remained at 490 nm (Fig. S2† inset). A maximum shift of λ_{em} to 815 nm was found when the ratio was 0.9 : 3.1 (Au : Ag) (Fig. 1, S2†). However, in this ratio the fluorescence intensity was found to be very low.

Subsequently, we carried out two series of experiments. In the first series, with increasing concentration of Ag (0.2 mM, 0.9 mM, 1.1 mM, 1.6 mM and 2.0 mM) at a fixed Au concentration of 2.3 mM, λ_{ems} was found at 608 nm, 655 nm, 658 nm, 660 nm and 718 nm, respectively (Fig. 2a). However, the red shift of the emission maxima was associated a with quenching of fluorescence intensity, particularly at a high concentration of Ag. In the second series, for a fixed Ag concentration of 2.0 mM, gradual increases of Au concentration (from 0.7 mM to 2.3 mM) resulted in a steady blue shift from 812 nm to 718 nm (Fig. 2b).

We then used time resolved fluorescence spectroscopy which suggested a bi-exponential decay for the monometallic Au NCs. The lifetime components of 1.74 ns (19.26%) and 261 ns (80.74%) were observed in this system, which resulted in an

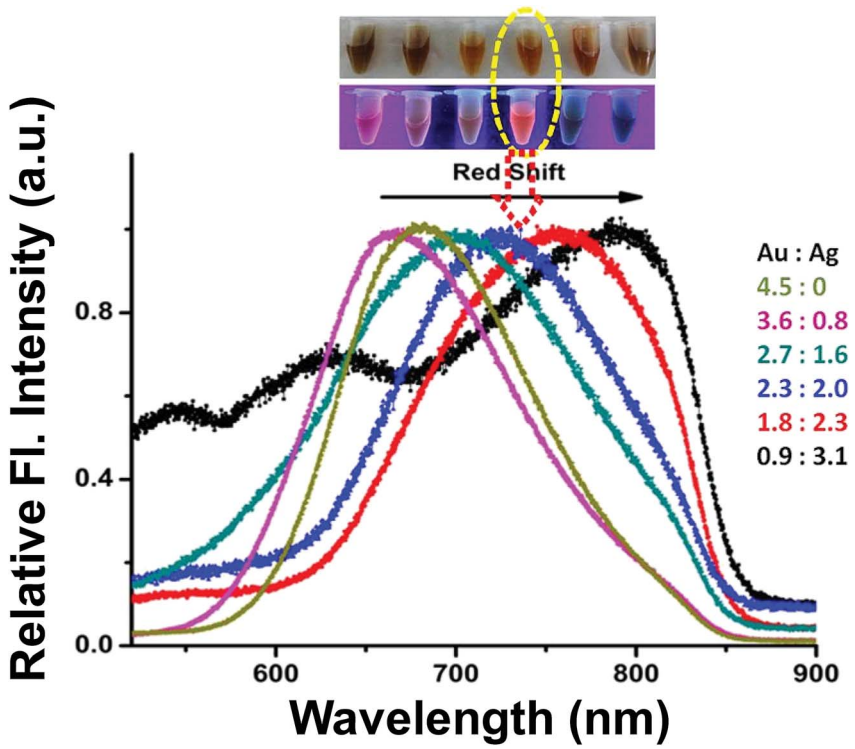

Fig. 1 Normalised fluorescence intensity *vs.* wavelength plot of Au–Ag@BSA NCs with different molar ratios of Au and Ag. This figure suggested a gradual red shift of emission spectra with increasing concentration of Ag. The red arrow indicates the composition of our interest as it showed significant intensity in the NIR region (Au : Ag = 2.3 : 2.0).

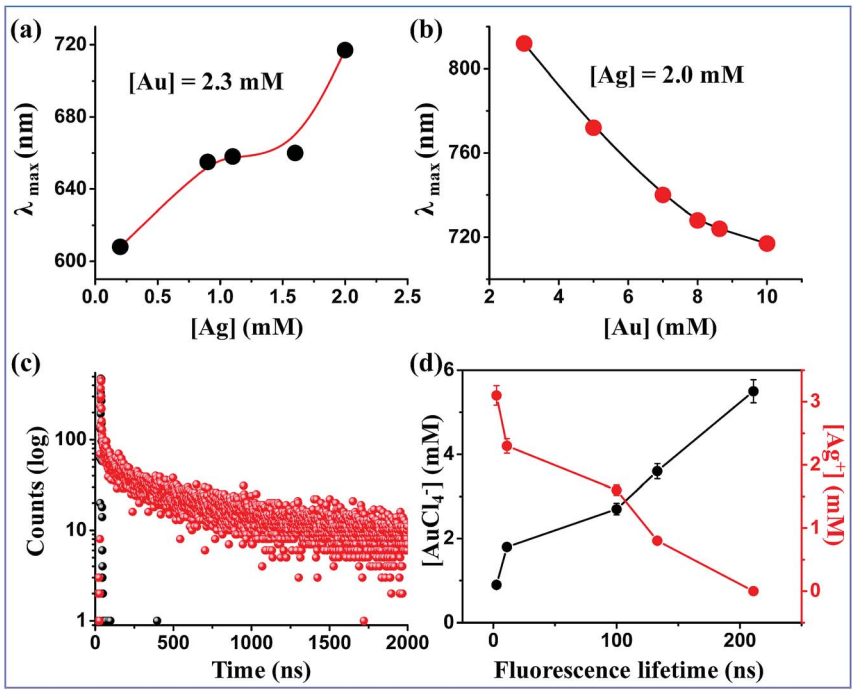

Fig. 2 (a) Change in the wavelength of Au–Ag@BSA NCs as observed from fluorescence emission spectra with varying Ag concentration keeping the Au concentration fixed at 2.3 mM; (b) change in wavelength of Au–Ag@BSA NCs as observed from fluorescence emission spectra with varying Au concentration keeping the Ag concentration fixed at 2.0 mM; (c) fluorescence lifetime spectra of $(Au–Ag@BSA)_{opt}$ NCs where the Au : Ag molar ratio was 2.3 : 2.0; (d) changes in fluorescence lifetime with respect to the concentration of Au and Ag.

average life time of 211 ns (Fig. 2c). The nanosecond lifetime values exhibited by monometallic Au NCs are due to different electronic transitions of the Au core, such as sp → sp and sp → d.[28] In contrast, several Au NCs are known in the literature, which show longer lifetime components (>100 ns). This long lifetime implies probable existence of ligand to metal charge transfer. We found that increasing the concentration of Ag caused gradual decrease in the long lifetime component with a decrease in the average lifetime (Table S2,† Fig. 2d). This happens presumably because of a compromised ligand to metal charge transfer in the bimetallic NCs. An optimized Au : Ag ratio of 2.3 : 2.0 was found to produce NIR emission at 718 nm with an acceptably high fluorescence QY of 42%. It exhibited an average lifetime of 14.2 ns. NCs synthesized under this optimized condition (referred to be $(Au–Ag@BSA)_{opt}$ NCs now onwards) were used for further studies unless stated otherwise.

Characterization of $(Au–Ag@BSA)_{opt}$ NCs

Detailed characterization of $(Au–Ag@BSA)_{opt}$ NCs was carried out using different methods. A strong red fluorescence with the emission maximum at 718 nm (λ_{ex} = 490 nm) was obtained from our synthesized $(Au–Ag@BSA)_{opt}$ NCs (Au : Ag = 2.3 : 2.0) (blue curve in Fig. 1). High resolution transmission electron microscopy (HR-TEM) showed an average diameter of 2.4 nm (±0.45) for $(Au–Ag@BSA)_{opt}$ NCs (Fig. S3a†). This measurement typically show a slightly larger average size as a result of high-energy electron beam-induced melting of the metal core.[16,29,30] This result was also complemented by the DLS size distribution of $(Au–Ag@BSA)_{opt}$ NCs (Fig. S3b†). EDAX analysis of $(Au–Ag@BSA)_{opt}$ NCs showed the presence of expected elements of Au, Ag and S (Fig. S3c,† inset table). The zeta potential value of the $(Au–Ag@BSA)_{opt}$ NCs was found to be −27 mV (Fig. S1b†).

The composition of the as-prepared $(Au–Ag@BSA)_{opt}$ NCs was estimated by measuring the mass difference between $(Au–Ag@BSA)_{opt}$ NCs and the free BSA protein (Fig. S4†). MALDI revealed the presence of a peak at an m/z value of 73.6 kDa for $(Au–Ag@BSA)_{opt}$ NCs. A second peak at an m/z value of 66.5 kDa was observed because of free BSA under the reaction condition (pH 11). The mass difference of 7100 Da (mass of Au × 32 = 197 × 32 = 6304, mass of Ag × 7 = 108 × 7 = 756, and total = 7060–7100 Da) between $(Au–Ag@BSA)_{opt}$ NCs and BSA matched well with the atomic composition of $Au_{32}Ag_7$@BSA NCs as also observed from the EDAX data (Fig. S3d†). It is known that clusters with certain special numbers of atoms (magic numbers) are more abundant than others. Au_{39} has been reported to be a magic number in glutathione capped NCs.[31–33] Since $Au_{32}Ag_7$ contains a magic number of atoms in its cluster core, this bimetallic nanocluster is expected to be stable.

X-ray photoelectron spectroscopy (XPS) was used to illustrate the oxidation states of the Au and Ag in $(Au–Ag@BSA)_{opt}$ NCs. Au atoms in the NCs were found to be predominantly in the reduced state (Au^0) owing to the considerably low binding energy of Au $4f_{7/2}$ of ~83.5 eV and for Au $4f_{5/2}$ of 87.1 eV (Fig. S5a†). It has been reported that binding energy values of the Au $4f_{7/2}$ and Au $4f_{5/2}$ levels for BSA–Au NCs are typically near 84.01 and 87.81 eV, respectively.[34] In the presence of a Au and Ag molar concentration ratio of 2.3 : 2.0, the Ag 3d spectrum

(Fig. S5b†) was resolved into two spin–orbit components at 366.6 eV and 372.5 eV, which was consistent with the previous result obtained for Ag NCs.[35] We assigned these peaks to the Ag $3d_{5/2}$ and Ag $3d_{3/2}$, respectively. It was noted that there was not much difference in BE between Ag(0) and Ag(I) states due to the close proximity of their binding energies. In this context, it is to be mentioned that the BE of Au $4f_{7/2}$ (83.3 eV) is lower than the BE of the Au(0) film (84.0 eV),[26] which implies that Au atoms are negatively charged in the $(Au–Ag@BSA)_{opt}$ NCs. Again, the BE of Ag $3d_{5/2}$ (366.6 eV) was lower than that of the Ag(0) film (367.7 eV) indicating the positive charge of the Ag atoms. These results suggested that some charge transfer occurred in $(Au–Ag@BSA)_{opt}$ NCs from Ag with an electronegativity of 1.93 to Au, which has an electronegativity of 2.54.[24,36] In addition, BE peaks for sulphur $2p_{3/2}$ appeared at 161.7 and 167.2 eV (Fig. S6†), which can be attributed to the oxidized states of S. The peak at 161.7 eV corresponded to the covalent interaction of Au NCs with the SH groups of the Cys residue of the protein.

The stability of $(Au–Ag@BSA)_{opt}$ NCs was investigated under different experimental conditions. First, the addition of excess EDTA to the $(Au–Ag@BSA)_{opt}$ NC solution did not result in any change in the fluorescence intensity (Fig. S7a†), indicating the absence of free Ag^+ in bimetallic NCs. Second, the emission intensity of $(Au–Ag@BSA)_{opt}$ NCs remained stable even in solutions with high ionic strength (*e.g.*, 500 mM NaCl, Fig. S7a†). This observation is similar to that reported by the Xie group.[24] In addition, there was no change in fluorescence for $(Au–Ag@BSA)_{opt}$ NCs detected in the pH values ranging from 5.0 to 9.0 (Fig. S7b†). Furthermore, no change in fluorescence was detected by storing $(Au–Ag@BSA)_{opt}$ NCs in darkness for ten months (Fig. S7c†).

Doping of foreign metals can cause alloy nanoclusters to possess different geometrical and electronic structures compared to their mono-metal counterparts.[37] However, it is difficult to resolve the exact crystalline structure of these $(Au–Ag@BSA)_{opt}$ NCs since nanocluster growth occur *in situ* within the BSA template. While it is difficult to determine the exact factors which are responsible for the observed fluorescence behaviour, both the metal core and the ligands are expected to contribute. It has been reported that Ag atom doping in $Au_{25}(SG)_{18}$ nanoclusters blue shifts the absorption onset.[36,38] Doping of Ag heteroatoms increase the LUMO energy while leaving the HOMO energy unaffected, and this perturbation shifts characteristic absorption to higher energy.[38,39] Moreover, heteroatom-induced splitting of discrete energy levels also introduces new features in the $(Au–Ag@BSA)_{opt}$ NCs spectrum profile. In any case, a defined understanding of the modulation of HOMO–LUMO absorption would not be simple to understand. The modulation of the emission properties due to Ag heteroatom doping is expected to be directionless and size dependent.[26] In our study, the fluorescence red shift may be due to either MLCT within the metal and surrounding protein residues or MMCT within Au and Ag atoms. The metal–metal interactions are possibly formed by weaker van der Waals forces and the charge transfer component that dominated the excited state in the former is reduced.[5]

In our recent study, we reported that BSA fibril templated Au NCs showed a significant red shift of the emission maxima (~25 nm) when compared to the fluorescence properties of native BSA protected Au NCs.[16] In the present work, we showed that doping of Ag atoms into the Au matrix resulted in even more red shifts to the NIR region compared to pure Au nanoclusters prepared either in BSA or fibrillated BSA templates.

Detection of Pb^{2+} ions using $(Au–Ag@BSA)_{opt}$ NCs

The second objective of this study was to explore applications of the optimized $(Au–Ag@BSA)_{opt}$ NC system in detecting low concentrations of Pb^{2+} in both *in vitro* and *in cell* samples. As mentioned before, we aimed to obtain a NC system which would provide a metal induced increase (and not a decrease) facilitating image acquisitions for *in cell* studies. Interestingly, upon gradual addition of Pb^{2+} onto $(Au–Ag@BSA)_{opt}$ NCs, we observed a large increase in fluorescence intensity (Fig. 3a) at 718 nm, while non-optimized Au–Ag systems (in which the Au : Ag ratio was different from 2.3 : 2.0) showed either no change or quenching (Fig. S8a–d†). Fig. S8† clearly emphasizes the importance of ratio optimization to develop a bimetallic system depending on the intended applications. No significant change in shape of the nanocluster fluorescence spectrum or shift in the emission maxima was observed for $(Au–Ag@BSA)_{opt}$ NCs due to Pb^{2+} binding (Fig. 3a). The average lifetime of the $(Au–Ag@BSA)_{opt}$ NCs as determined by the time resolved fluorescence measurements increased to 111.3 ns in the presence of added Pb^{2+} (Fig. 3b, Table 1). Decay patterns of $(Au–Ag@BSA)_{opt}$ NCs were found to be bi-exponential both in the absence and presence of Pb^{2+}.

The probable mechanism for Pb^{2+} sensing by $(Au–Ag@BSA)_{opt}$ NCs would involve metallophilic interaction between Pb^{2+} ($5d^{10}$) and $Au^+(5d^{10})$–Ag^+ ($4d^{10}$).[40,41] To understand the selectivity and specificity of $(Au–Ag@BSA)_{opt}$ NCs, series of fluorescence titrations were carried out using different transition metal ions. Interestingly, no significant change in fluorescence intensity was observed for other metal ions (K^+, Na^+, Li^+, As^{3+}, Hg^{2+}, Al^{3+}, Cd^{2+}, Co^{2+}, Cr^{3+}, Cu^{2+}, Fe^{2+}, Fe^{3+}, Mn^{2+}, Ni^{2+} and Zn^{2+}) which is in contrast with Pb^{2+}, where the fluorescence intensity of the nanocluster increased significantly (Fig. 3c).

The limit of detection (LOD) was calculated from the slope of the plot of intensity *vs.* concentration of Pb^{2+} (Fig. 3d). The LOD value was estimated using the assumption of LOD equal to $3\sigma/b$, where σ is the standard deviation of intensity residuals and b is the slope of the calibration curve. Our observed detection limit was 96 nM. Table S3† compares a list of available reports of NC based sensors towards Pb^{2+} detection. While the LOD of the present method is competitive in comparison to those of the previous reports, ours is the only NC based material with fluorescence enhancement in the NIR region to the best of our knowledge.

In cell detection of Pb^{2+} ions

To assess the suitability of $(Au–Ag@BSA)_{opt}$ NCs in detecting Pb^{2+} within the confines of the cell cytosol an essential step is to comprehend the effect of extraneous $(Au–Ag@BSA)_{opt}$ NCs on

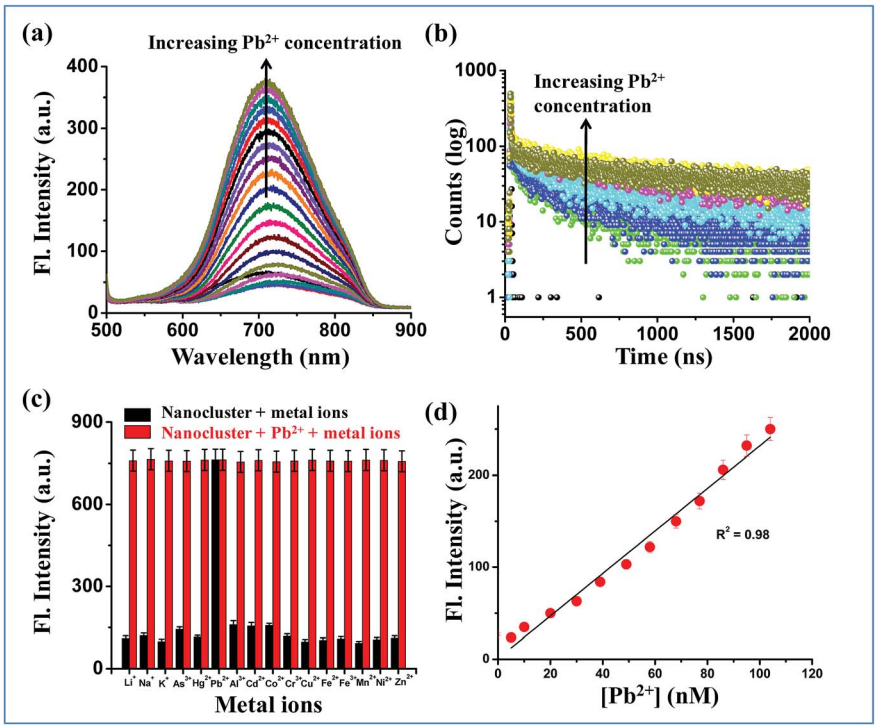

Fig. 3 (a) Fluorescence intensity enhancement with increasing concentration of Pb^{2+}; (b) increase in fluorescence lifetime with increasing concentration of Pb^{2+}; (c) bar plots presenting the extent of fluorescence enhancement of $(Au–Ag@BSA)_{opt}$ NCs in the presence of different metal ions; (d) plot of fluorescence intensity against the concentration of Pb^{2+} showing the limit of detection (LOD).

Table 1 Changes in τ_1 and τ_2 values of $(Au–Ag@BSA)_{opt}$ NCs with gradual addition of Pb^{2+}

$[Pb^{2+}]$ (μM)	τ_1 (ns)	τ_2 (ns)	τ_{av} (ns)	χ^2
0	1.04	98.6	14.2	1.25
48	1.18	92.2	9.66	1.30
95	13.4	53.9	17.1	1.24
180	0.80	105.0	17.4	1.14
260	0.85	118.7	33.6	1.04
330	1.00	143.3	111.3	1.06

cell health. Furthermore, an effective idea about the dosage and its concomitant effect on cell viability stands extremely important. Hence, the MTT assay was performed under the treatment conditions spanning over a wide range of $(Au–Ag@BSA)_{opt}$ NC concentrations (500 nM to 1600 μM) for a time frame of 24 h. The HeLa cell line was chosen as the model cell system for all our subsequent cell-based experiments. The MTT assay suggested that over 98% of the cells were viable when treated with 500 nM concentration NCs whereas ~90% or more viable cells were present over the concentration range 1–10 μM. Again, a little decrease in viable cell population was observed for the

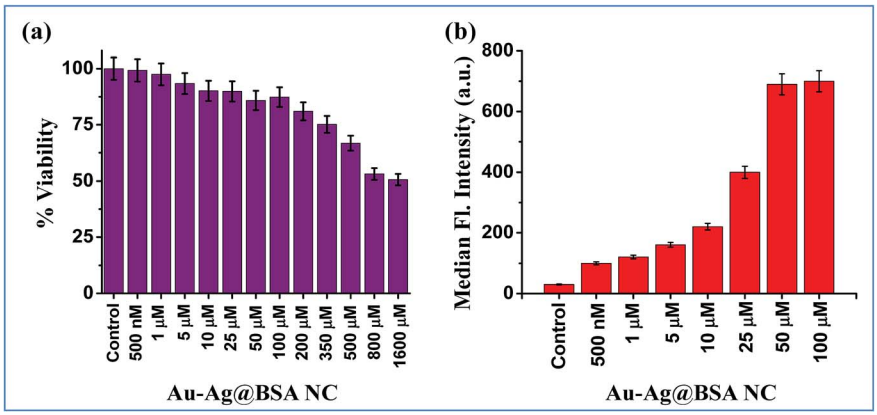

Fig. 4 (a) MTT assay showing the percentage of viable cell populations in the presence of different concentrations of $(Au–Ag@BSA)_{opt}$ NCs; (b) bar plot presenting the extent of permeation of $(Au–Ag@BSA)_{opt}$ NCs at different concentrations as obtained from FACS.

concentration range 25–350 μM (cell viability from 85 to 75%) (Fig. 4a). Further, a relatively sharp decrease of cell viability was found when there is a $(Au–Ag@BSA)_{opt}$ NC concentration hike from 500 to 1600 μM (cell viability 65–50%). Data reflected the minimum effect of NCs on the cell viability for a broad range of concentrations ranging below 50 μM. Based on the above observation, we further explored the effectiveness of this bimetallic nanocluster towards the detection of Pb^{2+} in cellular environments. Permeation assay guided by flow cytometry was carried out to have a quantitative understanding of the concentration of $(Au–Ag@BSA)_{opt}$ NCs which effectively permeates from the medium to the cell cytosol and can be further considered as the effective probe concentration. For all these assays we preferred to select concentrations below 50 μM (as concentrations <50 μM showed a cell viability of more than around 80 percent). Our FACS data reveal 50 μM $(Au–Ag@BSA)_{opt}$ NCs show the highest uptake (Fig. 4b), as evident from the fluorescent signals obtained from the sorted cells. Thus, for the subsequent imaging studies we went ahead with 50 μM $(Au–Ag@BSA)_{opt}$ NC concentration as it was the perfect choice for efficient permeation and high cell viability.

Live cell confocal imaging using a Leica TCS-SP8 confocal microscope revealed a notable extent of $(Au–Ag@BSA)_{opt}$ NC permeation upon treatment of HeLa cells with 50 μM nanoclusters (Fig. 5). Pixel distribution and quantification from the live cell image showed an average fluorescence intensity of around 10 units (A.U) as confirmed from the 3D interactive surface plots of the ImageJ ensemble (Fig. 5c). The post-permeation residence of NCs inside the cells does not create cell stress. $(Au–Ag@BSA)_{opt}$ NCs were observed in the cell cytosol with insignificant alteration in cell shape. Next, an exogenous source of Pb^{2+} was introduced to $(Au–Ag@BSA)_{opt}$ NC treated HeLa cells for semi-quantitative measurement of the intracellular Pb^{2+} level. A significant rise of fluorescence intensity was observed upon treating the cells with 20 μM Pb^{2+} in the culture media for 15 min at 37 °C. A 3D interactive surface plot also confirmed the enhancement of signal up to an average intensity of 18 A.U (Fig. 5d). Our observation revealed the specific interactions between $(Au–Ag@BSA)_{opt}$ NCs and Pb^{2+} resulting in the fluorescence enhancement.

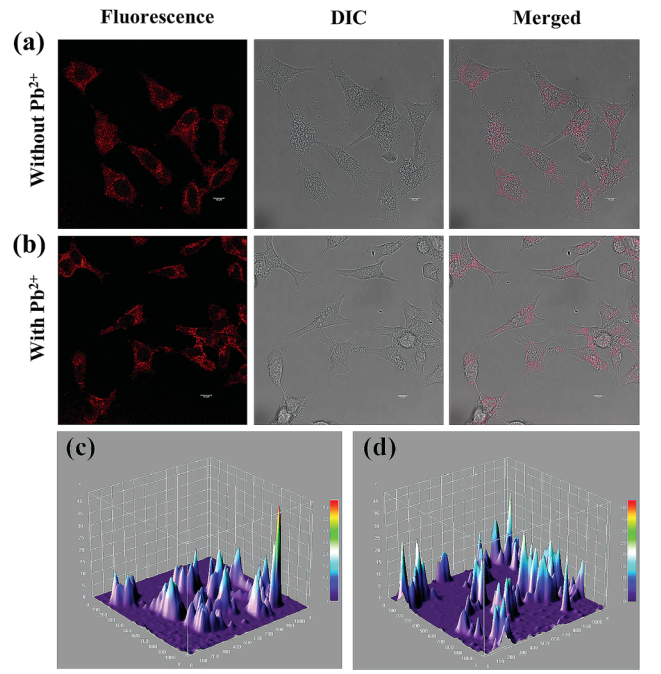

Fig. 5 Confocal imaging of HeLa cells: fluorescence, DIC and merged images of HeLa cells (a) without and (b) with treatment of Pb^{2+} ions (50 μM $(Au–Ag@BSA)_{opt}$ NCs for 20 min incubation); 3D surface plot of $(Au–Ag@BSA)_{opt}$ NC permeation, that is, the heat map in (c) absence and (d) presence of Pb^{2+}.

Real sample analysis

To test the applicability of the as-prepared NCs for Pb^{2+} detection, we collected water samples from different local sources. These include samples from a neighbourhood pond, tap water supplied by the Kolkata Municipal Corporation, and the same tap water samples, which were subjected to purification by the reverse osmosis method. Table 2 shows the results, which suggested that all three sources were safe at least in terms of Pb^{2+} content. Subsequently, we spiked all these three water samples with Pb^{2+} of different concentrations, to determine if other dissolved substances present in these samples (which would be very different for these three sources) would interfere with the fluorescence properties and LOD of our detection. The

Table 2 Detection of Pb^{2+} in natural samples using the standard addition method. The term 'Spiked' denotes the addition of different concentration of Pb^{2+}. "Recovery" denotes the percentage of lead detection by $(Au–Ag@BSA)_{opt}$ NCs with respect to the added Pb^{2+}. RSD is the relative standard deviation

Sample	Detected (nM)	Spiked (nM)	Found (nM)	Recovery	RSD
Tap water (Kolkata Municipal Corporation)	ND	100	98.7	98.7 ± 0.2	0.38
	ND	200	195.1	97.5 ± 0.5	1.01
	ND	300	305.0	101.6 ± 1.1	1.15
Neighborhood pond	ND	100	96.0	96.0 ± 0.1	1.07
	ND	200	185.0	92.0 ± 1.6	1.28
	ND	300	287.5	95.3 ± 0.8	0.83
Drinking water (reverse osmosis)	ND	100	97.8	97.8 ± 0.1	1.21
	ND	200	198.0	99.0 ± 0.6	1.36
	ND	300	307.6	102.5 ± 0.7	0.69

pond and tap would contain higher concentrations of organic and chlorine rich substances, respectively, while the reverse osmosis purified water would contains minimum dissolved substances. Fig. S9† suggests no significant differences in fluorescence characteristics. The water samples were spiked with standard solutions containing different concentrations of Pb^{2+}. The results are summarized in Table 2, which indicate that the as-prepared fluorescent nanoclusters can be used practically to detect Pb^{2+} in environmental samples.

Conclusions

In summary, the present work showed tuning of NIR fluorescence of Au–Ag bimetallic nanoclusters when synthesized using a BSA protein scaffold. The emission wavelength within the NIR region is highly desirable for diverse biological applications. We showed further that by varying the Au : Ag molar ratio, emission maxima can be shifted up to 815 nm. The probability of further enhancement of fluorescence intensity of these nanoclusters at these metal ratios by tuning metal-to-ligand or ligand-to-metal charge transfer pathways can open up more advanced investigation possibilities $(Au–Ag@BSA)_{opt}$ NCs exhibit appreciable stability at different solution pH and in the presence of chelating agents (EDTA) and salt (NaCl). In addition, these bimetallic NCs were found to be useful to detect toxic Pb^{2+} ions (LOD $\sim$ 96 nM). As a concluding remark, we propose these NIR fluorescent $(Au–Ag@BSA)_{opt}$ NCs to be used as a potential sensor towards the detection of toxic Pb^{2+} in biological environments as well as in real samples.

Conflicts of interest

There are no conflicts to declare.

Acknowledgements

Author S. C. acknowledges DST (SERB) for providing NPDF (File no. PDF/2017/000453). The authors A. S. and S. C. acknowledge UGC for providing SRF. The author I. N. acknowledges CSIR for providing SRF. The author D. S. acknowledges DST for the senior research fellowship under the INSPIRE scheme. The authors acknowledge the technical support of Tanmoy Dalui for FACS experiments. The authors thank the director of CSIR-IICB for his support and encouragement.

References

1 P. K. Sarkar, A. Halder, N. Polley and S. K. Pal, Development of highly selective and efficient prototype sensor for potential application in environmental mercury pollution monitoring, *Water, Air, Soil Pollut.*, 2017, **228**, 314.
2 M. Li, H. Gou, I. A. Ogaidi and N. Wu, Nanostructured Sensors for Detection of Heavy Metals: A Review, *ACS Sustainable Chem. Eng.*, 2013, **1**, 713–723.
3 H. N. Kim, W. X. Ren, J. S. Kim and J. Yoon, Fluorescent and colorimetric sensors for detection of lead, cadmium, and mercury ions, *Chem. Soc. Rev.*, 2012, **41**, 3210–3244.
4 T. Rasheed, M. Bilal, F. Nabeel, H. M. Iqbal, C. Li and Y. Zhou, Fluorescent sensor based models for the detection of environmentally-related toxic heavy metals, *Sci. Total Environ.*, 2018, **615**, 476–485.
5 B. Paramanik and A. Patra, Fluorescent Au–Ag alloy clusters: synthesis and SERS applications, *J. Mater. Chem. C*, 2014, **2**, 3005–3012.
6 T. Chen, S. Yang, J. Chai, Y. Song, J. Fan, B. Rao, H. Sheng, H. Yu and M. Zhu, Crystallization-induced emission enhancement: A novel fluorescent Au–Ag bimetallic nanocluster with precise atomic structure, *Sci. Adv.*, 2017, **3**, e1700956.
7 J. S. Mohanty, P. L. Xavier, K. Chaudhari, M. S. Bootharaju, N. Goswami, S. K. Pal and T. Pradeep, Luminescent, bimetallic Au–Ag alloy quantum clusters in protein templates, *Nanoscale*, 2012, **4**, 4255–4262.
8 T. Udayabhaskararao and T. Pradeep, New protocols for the synthesis of stable Ag and Au nanocluster molecules, *J. Phys. Chem. Lett.*, 2013, **4**, 1553–1564.
9 D. Mishra, S. Wang, Z. Jin, E. Lochner and H. Mattoussi, Highly Fluorescent $Au_{25-x}Ag_x$ Nanoclusters Protected with Poly(ethylene glycol)-and Zwitterion-Modified Thiolate Ligands, *ChemRxiv*, 2018, DOI: 10.26434/chemrxiv.6987479.v1.
10 S. Link, A. Beeby, S. FitzGerald, M. A. El-Sayed, T. G. Schaaff and R. L. Whetten, Visible to infrared luminescence from a 28-atom gold cluster, *J. Phys. Chem. B*, 2002, **106**, 3410–3415.
11 J. M. Liu, J. T. Chen and X. P. Yan, Near infrared fluorescent trypsin stabilized gold nanoclusters as surface plasmon enhanced energy transfer biosensor and *in vivo* cancer imaging bioprobe, *Anal. Chem.*, 2013, **85**, 3238–3245.
12 G. Pramanik, J. Humpolickova, J. Valenta, P. Kundu, S. Bals, P. Bour, M. Dracinsky and P. Cigler, Gold nanoclusters with bright near-infrared photoluminescence, *Nanoscale*, 2018, **10**, 3792–3798.
13 S. Pang and S. Liu, Lysozyme-stabilized bimetallic gold/silver nanoclusters as a turn-on fluorescent probe for determination of ascorbic acid and acid phosphatase, *Anal. Methods*, 2017, **9**, 6713–6718.
14 B. A. Ashenfelter, A. Desireddy, S. H. Yau, T. Goodson III and T. P. Bigioni, Fluorescence from molecular silver nanoparticles, *J. Phys. Chem. C*, 2015, **119**, 20728–20734.
15 S. Chall, S. S. Mati, I. Das, A. Kundu, G. De and K. Chattopadhyay, Understanding the Effect of Single Cysteine Mutations on Gold Nanoclusters as Studied by Spectroscopy and Density Functional Theory Modeling, *Langmuir*, 2017, **33**, 12120–12129.
16 I. Nandi, S. Chall, S. Chowdhury, T. Mitra, S. S. Roy and K. Chattopadhyay, Protein Fibril-Templated Biomimetic Synthesis of Highly Fluorescent Gold Nanoclusters and Their Applications in Cysteine Sensing, *ACS Omega*, 2018, **3**, 7703–7714.
17 A. Sannigrahi, S. Chall, J. J. Jawed, A. Kundu, S. Majumdar and K. Chattopadhyay, Nanoparticle Induced Conformational Switch Between α-Helix and β-Sheet

Attenuates Immunogenic Response of MPT63, *Langmuir*, 2018, **34**, 8807–8817.

18 B. Paramanik, A. Kundu, K. Chattopadhyay and A. Patra, Study of binding interactions between MPT63 protein and Au nanocluster, *RSC Adv.*, 2014, **4**, 35059–35066.

19 X. Fu, T. Lou, Z. Chen, M. Lin, W. Feng and L. Chen, "Turn-on" fluorescence detection of lead ions based on accelerated leaching of gold nanoparticles on the surface of graphene, *ACS Appl. Mater. Interfaces*, 2012, **4**, 1080–1086.

20 W. Yantasee, C. Timchalk and Y. Lin, Microanalyzer for biomonitoring lead (Pb) in blood and urine, *Anal. Bioanal. Chem.*, 2007, **387**, 335–341.

21 Q. Zhou, Y. Lin, M. Xu, Z. Gao, H. Yang and D. Tang, Facile synthesis of enhanced fluorescent gold–silver bimetallic nanocluster and its application for highly sensitive detection of inorganic pyrophosphatase activity, *Anal. Chem.*, 2016, **88**, 8886–8892.

22 S. Chall, S. S. Mati, S. Konar, D. Singharoy and S. C. Bhattacharya, An efficient, Schiff-base derivative for selective fluorescence sensing of Zn^{2+} ions: quantum chemical calculation appended by real sample application and cell imaging study, *Org. Biomol. Chem.*, 2014, **12**, 6447–6456.

23 J. R. Lakowicz, *Principles of Fluorescence Spectroscopy*, Kluwer Academic/Plenum, New York, 1999.

24 J. Xie, Y. Zheng and J. Y. Ying, Protein-directed synthesis of highly fluorescent gold nanoclusters, *J. Am. Chem. Soc.*, 2009, **131**, 888–889.

25 X. Qu, Y. Li, L. Li, Y. Wang, J. Liang and J. Liang, Fluorescent gold nanoclusters: synthesis and recent biological application, *J. Nanomater.*, 2015, **2015**, 1–23.

26 H. Huang, H. Li, J. J. Feng and A. J. Wang, One-step green synthesis of fluorescent bimetallic Au/Ag nanoclusters for temperature sensing and *in vitro* detection of Fe^{3+}, *Sens. Actuators, B*, 2016, **223**, 550–556.

27 C. Kumara and A. Dass, Au–Ag alloy nanomolecules with 38 metal atoms, *Nanoscale*, 2012, **4**, 4084–4086.

28 Y. Lu and W. Chen, Sub-nanometre sized metal clusters: from synthetic challenges to the unique property discoveries, *Chem. Soc. Rev.*, 2012, **41**, 3594–3623.

29 Y. Wang, W. Liang and C. Geng, Coalescence behavior of gold nanoparticles, *Nanoscale Res. Lett.*, 2009, **4**, 684.

30 J. Li, Z. Wang, C. Chen and S. Huang, Atomic-scale observation of migration and coalescence of au nanoclusters on YSZ surface by aberration-corrected STEM, *Sci. Rep.*, 2014, **4**, 5521.

31 Y. Negishi, Y. Takasugi, S. Sato, H. Yao, K. Kimura and T. Tsukuda, Magic-Numbered Au_n Clusters Protected by Glutathione Monolayers (n = 18, 21, 25, 28, 32, 39): Isolation and Spectroscopic Characterization, *J. Am. Chem. Soc.*, 2004, **126**, 6518–6519.

32 Y. Negishi, K. Nobusada and T. Tsukuda, Glutathione-Protected Gold Clusters Revisited: Bridging the Gap between Gold(I)-Thiolate Complexes and Thiolate-Protected Gold Nanocrystals, *J. Am. Chem. Soc.*, 2005, **127**, 5261–5270.

33 Y. Han, D. S. He, Y. Liu, S. Xie, T. Tsukuda and Z. Y. Li, Size and Shape of Nanoclusters: Single-Shot Imaging Approach, *Small*, 2012, **8**, 2361–2364.

34 Y. Zhang, H. Jiang, W. Ge, Q. Li and X. Wang, Cytidine-Directed Rapid Synthesis of Water-Soluble and Highly Yellow Fluorescent Bimetallic Au–Ag Nanoclusters, *Langmuir*, 2014, **30**, 10910–10917.

35 R. Kobayashi, Y. Nonoguchi, A. Sasaki and H. Yao, Chiral Monolayer-Protected Bimetallic Au–Ag Nanoclusters: Alloying Effect on Their Electronic Structure and Chiroptical Activity, *J. Phys. Chem. C*, 2014, **118**, 15506–15515.

36 D. R. Kauffman, D. Alfonso, C. Matranga, H. Qian and R. A. Jin, Quantum Alloy: The Ligand-Protected $Au_{25-x}Ag_x(SR)_{18}$ Cluster, *J. Phys. Chem. C*, 2013, **117**, 7914–7923.

37 K. D. M. Weerawardene and C. M. Aikens, Origin of Photoluminescence of $A_{g25}(SR)_{18}$-Nanoparticles: Ligand and Doping Effect, *J. Phys. Chem. C*, 2018, **122**, 2440–2447.

38 S. K. Katla, J. Zhang, E. Castro, R. A. Bernal and X. Li, Atomically Precise $A_{u25}(SG)_{18}$ Nanoclusters: Rapid Single-Step Synthesis and Application in Photothermal Therapy, *ACS Appl. Mater. Interfaces*, 2017, **10**, 75–82.

39 H. Yao, R. Kobayashi and Y. Nonoguchi, Enhanced Chiroptical Activity in Glutathione-Protected Bimetallic $(Au–Ag)_{18}$ Nanoclusters with Almost Intact Core–Shell Configuration, *J. Phys. Chem. C*, 2016, **120**, 1284–1292.

40 L. Ou, X. Li, H. Liu, L. Li and X. Chu, Poly(thymine)-templated fluorescent copper nanoparticles for ultrasensitive label-free detection of Pb^{2+} ion, *Anal. Sci.*, 2014, **30**, 723–727.

41 D. Bain, S. Maity, B. Paramanik and A. Patra, Core-Size Dependent Fluorescent Gold Nanoclusters and Ultrasensitive Detection of P^{b2+} Ion, *ACS Sustainable Chem. Eng.*, 2018, **6**, 2334–2343.